Letter

Unified characterization for higher-order topological phase transitions

Wei Jia [1,2] Xin-Chi Zhou [1,2] Lin Zhang [3] Long Zhang [4] and Xiong-Jun Liu [1,2,5,*]

[1] *International Center for Quantum Materials and School of Physics, Peking University, Beijing 100871, China*

[2] *Hefei National Laboratory, Hefei 230088, China*

[3] *ICFO-Institut de Ciencies Fotoniques, The Barcelona Institute of Science and Technology, Av. Carl Friedrich Gauss 3, 08860 Castelldefels (Barcelona), Spain*

[4] *School of Physics and Institute for Quantum Science and Engineering, Huazhong University of Science and Technology, Wuhan 430074, China*

[5] *International Quantum Academy, Shenzhen 518048, China*

(Received 26 September 2022; accepted 13 April 2023; published 15 May 2023)

Higher-order topological phase transitions (HOTPTs) are associated with closing either the bulk energy gap (type-I) or boundary energy gap (type-II) without changing symmetry, and conventionally, both transitions are captured in real space and characterized separately. Here, we propose a momentum-space topological characterization of HOTPTs which unifies both types of topological transitions and enables a precise detection by quench dynamics. Our unified characterization is based on a correspondence between mass domain walls on real-space boundaries and higher-order band-inversion surfaces (BISs) which are characteristic interfaces in the momentum subspace. Topological transitions occur when momentum-space topological nodes, dubbed *higher-order topological charges*, cross the higher-order BISs after proper projection. Particularly, the bulk (boundary) gap closes when all (part of) topological charges cross the BISs, characterizing type-I (type-II) HOTPTs. These distinct dynamical behaviors of higher-order topological charges can be feasibly measured from quench dynamics driven with control in experiments. Our work opens an avenue to characterize and detect the two types of HOTPTs within a unified framework and shall advance research in both theory and experiments.

DOI: 10.1103/PhysRevResearch.5.L022032

I. INTRODUCTION

Higher-order topological phases [1–6] have drawn widespread attention in recent years. These topologically nontrivial phases generalize the well-known bulk-boundary correspondence, so that a d-dimensional (dD) nth-order topological phase hosts gapless states in the $(d-n)$D boundary, while its higher-dimensional boundaries are gapped, rendering the key feature of rich topological states [7–33]. More recently, higher-order topological states have also been found in Floquet systems [34–36], non-Hermitian systems [37–40], interacting systems [41,42], and fractal systems [43,44].

Since the bulk, as well as partially the boundary, is gapped for higher-order topological states, higher-order topological phase transitions (HOTPTs) are associated with closing either the bulk (type-I) or boundary (type-II) energy gap without changing symmetry [45–56]. Currently, type-I and II HOTPTs are characterized by topological invariants defined on the bulk and Wannier bands [57], respectively. For instance, multipole moments [8] and bulk polarization [9] can only be applied to identify the type-I HOTPTs, while the nested Wilson loop [3] and Wannier band polarizations [52] are limited to the type-II HOTPTs. Nevertheless, when topological transitions occur, these invariants defined by the bulk and boundary properties are not unified and cannot fully capture all transitions [58–60]. Hence, the independent characterization cannot essentially describe HOTPTs and is not conducive to uncover higher-order topological states.

Meanwhile, the current characterizations bring difficulties for identifying both types of topological transitions in experiments [61–63]. Very recently, experimental realizations of higher-order topological states have been widely reported in cleaning synthetic systems in a controllable fashion [64–72]. The bulk physics can be conveniently simulated in synthetic systems like ultracold atoms [73–76], nitrogen-vacancy centers [77–79], and nuclear magnetic resonance [80,81], while classical simulators (such as phononic crystals [64], photonic crystals [65], and electric circuits [66]) provide ideal grounds to play with higher-order boundary modes. However, while having high controllability, it is still challenging to observe the two types of HOTPTs in these synthetic systems due to the lack of full manipulation and detection of both the bulk and boundary physics.

Motivated by these considerations, in this letter, we propose a unified characterization for both fundamental types of HOTPTs which goes beyond the traditional independent characterization and enables a feasible detection of HOTPTs

*xiongjunliu@pku.edu.cn

via quench dynamics. We first show a generic duality that, for a dD nth-order topological phase, the existence of $(d-n)$D gapless boundary states uniquely corresponds to the emergence of nth-order band-inversion surfaces (BISs) [82–91] which are $(d-n)$D interfaces in the momentum space characterizing where the energy bands cross and are inverted. Based on this nontrivial duality, topological phase transitions occur when higher-order topological charges cross higher-order BISs after proper projection, with type-I (or type-II) transitions being characterized by all (or part of) charges that pass through the BISs, providing an elegant and unified characterization of both types of HOTPTs. We finally show that both topological charges and BISs can be well measured in quantum quench experiments. Our work provides a way to simulate higher-order topological phases and detect HOTPTs.

II. DUALITY BETWEEN MASS DOMAIN WALL AND BIS

We start with deriving a duality between the mass domain wall (MDW) and BISs for a generic dD nth-order topological insulator (TI) captured by the Hamiltonian:

$$\mathcal{H}_{\mathbf{k}} = \sum_{j=1}^{d} h_j(k_j)\gamma_j + \sum_{l=1}^{n} h_{d+l}(k_1, \cdots, k_{d-l+1})\gamma_{d+l}, \quad (1)$$

where $\mathbf{k} = (k_1, k_2, \cdots, k_d)$ is the dD momentum. The Γ matrices obey the anticommutation relation of Clifford algebra [92,93] and can be regarded as (pseudo)spin operators. Here, we use the convention that $h_{j\leqslant d}$ denotes (pseudo)spin-orbit coupling coefficients, while h_{d+l} represents mass terms which include the Zeeman terms. Without mass terms, the Hamiltonian $\mathcal{H}_{\mathbf{k}}$ characterizes a massless Dirac semimetal. The mass term for $n = 1$ opens a bulk gap and gives the first-order topological model, such as the one-dimensional (1D) Su-Schrieffer-Heeger (SSH) chain [94] and the two-dimensional (2D) Haldane model [95]. For $n > 1$, the additional mass terms further open gaps on the boundary and give rise to the higher-order topological phases, including the second-order TIs with order-two symmetry [16] and the third-order TIs with inversion and reflection symmetries [87], where the crystalline symmetries determine the configurations of $(d-n)$D gapless boundary modes.

The boundary states of higher-order topological phases can be characterized through the dimensional reduction approach. Namely, the boundary states of an nth-order topological phase are obtained as Jackiw-Rebbi modes [96] by introducing Dirac MDWs into the $(d-n+1)$D boundary states of a $(n-1)$th-order topological phase [see Figs. 1(a) and 1(b)]. Accordingly, the $(d-n)$D MDWs in real space can correspond to the momentum-space $(d-n)$D closed surfaces with vanishing mass terms of the Hamiltonian in Eq. (1), defining the nth-order BISs $\mathcal{B}_n \equiv \{\mathbf{k}|h_{d+l} = 0, l = 1, 2, \ldots, n\}$ [see Fig. 1(c)]. This renders a MDW-BIS duality for the nth-order topological phases. Below, we briefly illustrate this duality of the Hamiltonian in Eq. (1). More details on the generic proofs are provided in the Supplemental Material [97].

We start from the first-order TIs ($n = 1$). The corresponding gapless surface states can be described as bound modes at the $(d-1)$D MDWs between the system and vacuum on real-space boundary. On the other hand, these surface states are

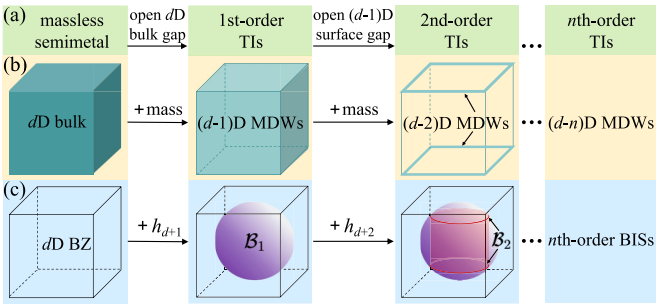

FIG. 1. Schematic of mass domain wall (MDW)-band-inversion surface (BIS) duality. (a) Construction of dD nth-order topological insulators (TIs) from massless semimetals by adding additional mass terms. (b) The corresponding $(d-n)$D MDWs in real space. (c) The corresponding nth-order BISs $\mathcal{B}_n$ in the Brillouin zone (BZ).

uniquely determined by the bulk topology, which is known to be further characterized by the $(d-1)$D first-order BIS $\mathcal{B}_1$ in momentum space with vanishing mass term $h_{d+1}(\mathbf{k}) = 0$ [82]. This renders the MDW-BIS duality for the first-order TIs. Further, the second-order topological phase is obtained when an additional mass term h_{d+2} is added to the Hamiltonian of first-order TIs; see Eq. (1). The condition $h_{d+2}(\mathbf{k}) = 0$ gives another first-order BIS, and its crossing with the BIS $\mathcal{B}_1$ results in a $(d-2)$D second-order BIS $\mathcal{B}_2$. The existence of $\mathcal{B}_2$ immediately implies that the additional mass term h_{d+2} must have sign changes after being projected onto the $(d-1)$D surface states of the first-order TIs [97]. Hence, the h_{d+2} term gaps out the $(d-1)$D surface states almost everywhere but leaves the MDWs on the $(d-2)$D boundary, yielding a second-order topological phase. Repeating the above procedures, we obtain all the higher-order topological phases, rendering the generic duality between the nth-order BISs and $(d-n)$D MDWs for the nth-order topological phases. This nontrivial duality reveals a correspondence between the momentum- space bulk physics and the real-space boundary physics. Moreover, it is also faithful for the higher-order topological phases with a stacking 1D SSH chain, such as the 2D and 3D BBH models [3,8] which can arrive at the Hamiltonian in Eq. (1) by rescaling the Γ matrices [32].

III. TOPOLOGICAL CHARACTERIZATION OF HOTPTS

We now develop the unified characterization of HOTPTs based on the above MDW-BIS duality. Here, a key idea is that an nth-order topological system can be equivalently transformed into the superposition of n effective first-order topological subsystems by using the dimensional reduction. Specifically, the $(d-i)$D MDWs are introduced to the $(d-i+1)$D boundary states by adding an additional mass term h_{d+i} to the Hamiltonian with $i = 1, 2, \ldots, n$, turning the $(i-1)$th-order topological phases into an ith-order topological phase. We treat the $(d-i+1)$D gapless boundary modes as a massless Dirac system, and then the MDWs of the ith-order topological phases are indeed the boundary states of an effective first-order $(d-i+1)$D gapped topological phase given by

$$\mathcal{H}_{\mathbf{k}^{(i-1)}} = \sum_{j\in D^{(i-1)}} h_j(k_j)\gamma_j^{(i-1)} + h_{d+i}[\mathbf{k}^{(i-1)}]\gamma_{d+i}^{(i-1)}, \quad (2)$$

with $D^{(i-1)}$ being a subset of $\{1, 2, \ldots, d\}$ with $(d-i+1)$ elements [97]. For these effective first-order topological subsystems, the $(d-i+1)$D momentum subspace $\mathbf{k}^{(i-1)}$ characterizes an effective $(d-i+1)$D Brillouin zone $\mathrm{BZ}^{(i-1)}$ obtained by projecting $\mathcal{B}_{i-1}$ onto the subspace spanned by all k_j, with the Γ matrices $\gamma_j^{(i-1)}$ being generally superpositions of the original ones [98].

With the above observation, the topological index $\mathcal{V}_n$ of the nth-order topological phase in Eq. (1) is then determined by all of the invariants w_i of the effective first-order topological Hamiltonian $\mathcal{H}_{\mathbf{k}^{(i-1)}}$, given by

$$\mathcal{V}_n = \mathrm{sgn}(|w_1 w_2 \cdots w_{n-1}|) w_n. \tag{3}$$

This can be easily understood in the process of constructing an nth-order topological phase from the $(n-1)$th-order TI with the topological index $\mathcal{V}_{n-1}$. The sign function $\mathrm{sgn}(|\mathcal{V}_{n-1}|) = 1$ (or 0) characterizes the presence (or absence) of the $(d-n+1)$D boundary states for the $(n-1)$th-order topological phase. As indicated by Eq. (2), the topology of the nth-order TI is inherited from these boundary modes [99,100] and is characterized by the invariant w_n, while the absence of these boundary states always leads to a trivial nth-order phase. Thus, the nth-order TI has the topological invariant $\mathcal{V}_n = \mathrm{sgn}(|\mathcal{V}_{n-1}|) w_n$. Repeating the same analysis for all $\mathcal{V}_{i\leqslant n-1}$ yields the topological index in Eq. (3).

The last step for the unified characterization is to represent w_i in terms of topological charges, which are dual to the BISs [101]. For the above effective first-order topological Hamiltonian, an sth-order topological charge $\mathcal{C}_{s,q}^{(i-1)} = \mathrm{sgn}\{J_{\mathbf{h}_{\mathrm{so}}}[\mathbf{k}_q^{(i-1)}]\}$ is a nodal point of (pseudo)spin-orbit coupled field $\mathbf{h}_{\mathrm{so}}[\mathbf{k}^{(i-1)}] = (h_1, h_2, \cdots, h_{d-i+2-s})$ at momenta $\mathbf{k}_q^{(i-1)}$ and quantified by Jacobian determinant $J_{\mathbf{h}_{\mathrm{so}}}[\mathbf{k}^{(i-1)}] \equiv \det(\partial h_{\mathrm{so},j'}/\partial k_{j'})$ [97,102]. Accordingly, the invariant w_i equals the total monopole charges enclosed by $\mathcal{B}_{\mathrm{proj},s}^{(i-1)} \equiv \{\mathbf{k}^{(i-1)} | h_{d-i+3-s} = \cdots = h_{d+i} = 0\}$, dubbed as the *projective* sth-order BISs. We then obtain

$$w_i = \sum_{q \in \bar{\mathcal{B}}_{\mathrm{proj},s}^{(i-1)}} \mathcal{C}_{s,q}^{(i-1)}, \tag{4}$$

where $\bar{\mathcal{B}}_{\mathrm{proj},s}^{(i-1)}$ is the momentum region enclosed by $\mathcal{B}_{\mathrm{proj},s}^{(i-1)}$ with $h_{d-i+3-s} < 0$. Unlike the higher-order BISs in the original bulk system, these projective higher-order BISs are defined in the effective $\mathrm{BZ}^{(i-1)}$ since $\mathcal{B}_{\mathrm{proj},s}^{(i-1)}$ is the projection of the ith-order BIS $\mathcal{B}_i$ onto $\mathrm{BZ}^{(i-1)}$. Equations (3) and (4) give the characterization for a broad class of higher-order topological phases with various lattice symmetries and described by the Hamiltonian in Eq. (1). We show later that, while the characterization is built on the topological indices w_i of the effective first-order topological system, it can be precisely measured in experiment by quench dynamics. We are now ready to write the unified characterization of the HOTPTs which must be associated with the change of w_i for one or multiple effective first-order topological subsystems in Eq. (2). Equivalently, in a HOTPT, the topological charges $\mathcal{C}_{s,q}^{(i-1)}$ must cross either the projective BIS $\mathcal{B}_{\mathrm{proj},s}^{(i-1)}$ or the border of $\mathrm{BZ}^{(i-1)}$ [see Fig. 2(a)]. Namely, a topological transition of nth-order phase

$$\mathcal{V}_n \xrightarrow[\text{type-I}(m=1)]{\text{type-II}(m>1)} \mathcal{V}_{m-1} \longrightarrow \mathcal{V}_p \tag{5}$$

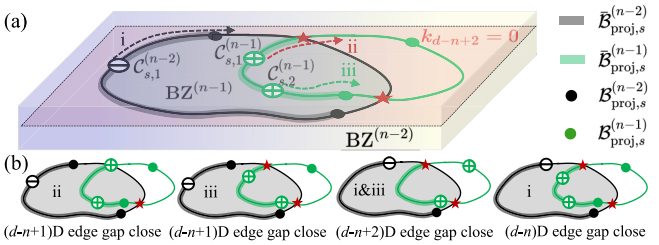

FIG. 2. Schematic of higher-order topological phase transitions (HOTPTs). (a) Behavior of topological charges in the phase transitions. Here, the charges cross either the projective band-inversion surfaces (BISs) [black (i) and green (iii) dots] or the border [red stars (ii)] of $\mathrm{BZ}^{(n-1)}$ (gray regions). The boundary gaps for $i < n-1$ are assumed to be open. (b) In (ii) or (iii), driving an $(n-1)$th-order topological phase, while (i) together with (iii) gives an $(n-2)$th-order topological phase. The nth-order topological phase shall remain unchanged when only (i) occurs.

occurs for i taking values from m to n, yielding at the critical point $(d-m+1)$D gapless boundaries characterized by $\mathcal{V}_{m-1}$ [see Fig. 2(b)]. For $m = 1$, all topological charges cross the projective BISs, and the bulk gap closes at the critical point, manifesting a type-I transition. For $m > 1$, only part of the topological charges crosses the projective BISs (or the border of effective BZ). Accordingly, the energy gap closes only for the $(d-m+1)$D boundaries parallel (or perpendicular) to the lower-dimensional $\mathrm{BZ}^{(m-1)}$, giving a type-II transition. This characterization also further precisely classifies the type-II transition into different m orders [97]. Moreover, it characterizes the HOTPT between an initial n-order phase and a final pth-order phase with $p \leqslant n$, given that $w_{i\leqslant p}$ is nonzero according to Eq. (3).

IV. DYNAMICAL DETECTION AND APPLICATION

We show now that the unified characterization can facilitate the precise detection of the HOTPTs and propose the applications based on quantum quenches. Our scheme is based on sequentially quenching of all the (pseudo)spin axes $\gamma_{\alpha=1,2,\ldots,d+n}$, while only measuring a single (pseudo)spin component γ_{d+1} in each quench. For this, we suddenly tune the Hamiltonian $\mathcal{H}_{\mathbf{k}} + \delta m_\alpha \gamma_\alpha$ from deep trivial regime $|\delta m_\alpha| \gg |h_\alpha|$ to topological regime $\delta m_\alpha = 0$. The time-averaged (pseudo)spin polarization γ_{d+1} after quench is given by $\overline{\langle \gamma_{d+1}(\mathbf{k}) \rangle}_\alpha \equiv \lim_{T\to\infty} \frac{1}{T} \int_0^T \mathrm{Tr}[\rho_\alpha \exp(\mathrm{i}\mathcal{H}_{\mathbf{k}} t) \gamma_\alpha \exp(-\mathrm{i}\mathcal{H}_{\mathbf{k}} t)] \mathrm{d}t$, where ρ_α is density matrix for the initial state. The projective BISs are determined as $\mathcal{B}_{\mathrm{proj},s}^{(i-1)} = \{\mathbf{k}^{(i-1)} | \overline{\langle \gamma_{d+1} \rangle}_{d-i+3-s} = \cdots = \overline{\langle \gamma_{d+1} \rangle}_{d+i} = 0\}$. The higher-order topological charge $\mathcal{C}_{s,q}^{(i-1)}$ is further detected by the dynamical field:

$$g_{j'} = -\lim_{\mathbf{k}^{(i-1)} \to \mathbf{k}_q^{(i-1)}} \frac{\mathrm{sgn}(h_\beta)}{\mathcal{N}_{\mathbf{k}^{(i-1)}}} \frac{\overline{\langle \gamma_{d+1} \rangle}_{j'} \overline{\langle \gamma_{d+1} \rangle}_\beta}{\overline{\langle \gamma_{d+1} \rangle}_{d+i}}, \tag{6}$$

for $s = 1$ with $\beta = d+i$ and $s > 1$ with $\beta = d-i+2-s$ since it can be shown that $g_{j'} = h_{\mathrm{so},j'}$ near the node point $\mathbf{k}_q^{(i-1)}$. Here, $\mathcal{N}_{\mathbf{k}^{(i-1)}}$ is a normalization factor. This dynamical detection scheme is highly feasible in experiment, as we demonstrate below.

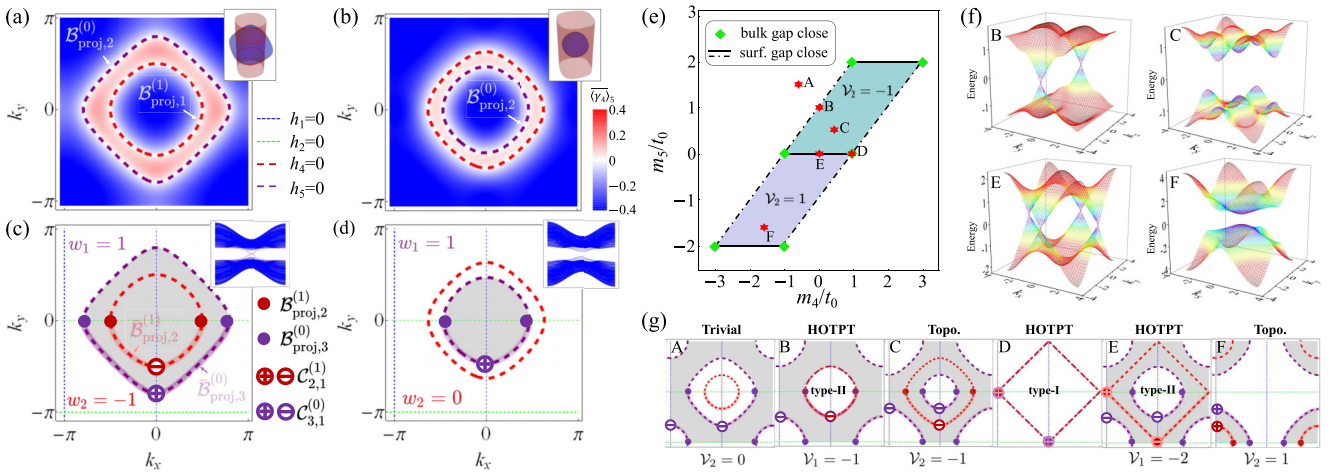

FIG. 3. Numerical results of three-dimensional (3D) second-order topological insulator (TI). (a) and (b) Time-averaged spin texture of $\overline{\langle\gamma_4(\mathbf{k})\rangle}_5$ at $k_z = 0$ by quenching each h axis from $\delta m_{1,2,3,4,5} = 30t_0$ to 0, where $(m_4, m_5) = (1.2t_0, t_0)$ is for (a) and $(2.1t_0, 0.6t_0)$ for (b). The vanishing polarization gives $\mathcal{B}^{(1)}_{\text{proj},1}$ and $\mathcal{B}^{(0)}_{\text{proj},2}$ in (a), while there is no $\mathcal{B}^{(1)}_{\text{proj},1}$ in (b) since the red dashed ring is not in $\text{BZ}^{(1)}$ (gray regions). The insets give $\mathcal{B}_1$ (a blue spherical) and $\mathcal{B}_2$ (two red rings) in original momentum space. (c) and (d) Configurations of the charges and band-inversion surfaces (BISs) for (a) and (b), where the insets are spectra with k_y and k_z open boundary conditions. (e) Phase diagram with the parameter points A–F (red stars). (f) The two lowest two-dimensional (2D) surface energies. (g) Configurations of the charges and BISs for A–F.

We exemplify the application of the unified characterization with a 3D second-order TI, constructed by adding a mass term into the 3D chiral TI [79,80], with the bulk Hamiltonian $\mathcal{H}_{\mathbf{k}} = \sum_{\alpha=1}^{5} h_\alpha \gamma_\alpha = h_1\sigma_x\tau_0 + h_2\sigma_y\tau_0 + h_3\sigma_z\tau_x + h_4\sigma_z\tau_z + h_5\sigma_z\tau_y$, where $h_{1,2,3} = t_{\text{so}} \sin k_{x,y,z}$, $h_4 = m_4 - t_0(\cos k_x + \cos k_y + \cos k_z)$, and $h_5 = m_5 - t_0(\cos k_x + \cos k_y)$. Here, σ and τ are both Pauli matrices and $k_{1,2,3} = k_{x,y,z}$. From the time-averaged spin texture shown in Fig. 3(a), we observe a ring-shaped projective BIS $\mathcal{B}^{(1)}_{\text{proj},1}$, manifesting the existence of the BIS $\mathcal{B}_2$ in original momentum space and identifying the emergence of hinge states according to the MDW-BIS duality. Moreover, one negative (positive) topological charge $\mathcal{C}^{(1)}_{2,1}$ [$\mathcal{C}^{(0)}_{3,1}$] is observed in the region $\bar{\mathcal{B}}^{(1)}_{\text{proj},2}$ [$\bar{\mathcal{B}}^{(0)}_{\text{proj},3}$] [see Fig. 3(c)], giving the topological invariant $\mathcal{V}_2 = -1$. Then the twofold degenerate zero energy states are localized at the hinges of the top and bottom surfaces along the z direction and protected by the C_4^z-rotation symmetry and the antireflection symmetry $\bar{\mathcal{R}}_j^\dagger \mathcal{H}_{k_j} \bar{\mathcal{R}}_j = -\mathcal{H}_{-k_j}$ along the $j = x, y, z$ axis. However, when $\mathcal{B}_2$ disappears [see Fig. 3(b)], there is no $\mathcal{B}^{(1)}_{\text{proj},1}$ or topological charge $\mathcal{C}^{(1)}_{2,q}$ in $\text{BZ}^{(1)}$ [see Fig. 3(d)]. Hence, we have $w_2 = 0$, and no zero energy state exists in the hinges.

Based on the MDW-BIS duality, the existence of $\mathcal{B}_2$ gives the second-order topological phase diagram $0 < |m_5| < 2t_0$ and $|m_4 - m_5| < t_0$, as shown in Fig. 3(e). One can see that the bulk energy bands become gapless at $(m_4, m_5) = \pm(3t_0, 2t_0), \pm(t_0, 2t_0), \pm(t_0, 0)$ (green squares), while the surface energy gap is only closed at $m_5 = 0, \pm 2t_0$ (solid lines) and $m_4 = m_5 \pm t_0$ (dot-dashed lines), which are confined to the real-space interfaces along and perpendicular to the z direction, respectively [97]. We shall choose two different parameter paths to observe the phase transitions. In path A-B-C-D [see Fig. 3(e)], there is one negative topological charge crossing the border (purple dashed curves) of $\text{BZ}^{(1)}$ [see Fig. 3(g)], and the surface energy gap closes in both xz and yz planes for B [see Fig. 3(f)]. This renders a type-II transition with $\mathcal{V}_2 = 0 \to \mathcal{V}_1 = -1 \to \mathcal{V}_2 = -1$ from A to C. As m_4 is further increased, all topological charges simultaneously move to the projective BISs for D, then the bulk energy gap closes, rendering a type-I transition. In another path C-E-F [see Fig. 3(e)], the surface energy gap closes in the xy plane for E. There is one negative topological charge crossing the projective BISs and changed into a positive topological charge. The higher-order topological transition occurs as $\mathcal{V}_2 = -1 \to \mathcal{V}_1 = -2 \to \mathcal{V}_2 = 1$. The unified characterization has explicit advantages that the topological phase transitions of different types can be resolved in quench dynamics.

V. DISCUSSION AND CONCLUSIONS

The unified characterization also shows that type-II transitions are further classified into different m orders which can be precisely determined by quench detection. In the Supplemental Material [97], we have presented more relevant examples for the 2D second-order and 3D third-order TIs, which further showcase the broad applicability of the unified characterization. Moreover, our unified theory may be applied to study Floquet higher-order phases and phase transitions, such as clarifying which type of phase transitions dominate the emergence of Floquet corner modes [103]. This shall further promote the study of topological phase transitions in Floquet higher-order systems.

In summary, we have shown a unified characterization in momentum space for HOTPTs and further proposed the detection by quench dynamics. The unified characterization is built on the MDW-BIS duality which relates the higher-order boundary modes in real space and the higher-order BISs with topological charges in the momentum space. The topological phase transitions of two types and various orders are

generically identified by the higher-order topological charges crossing over the BISs after proper projection, which can be precisely detected by quench dynamics. In this letter, we establish a unified and fundamental characterization of the higher-order topological phases and phase transitions, which shall advance further broad studies in theory and experiments.

ACKNOWLEDGMENTS

This letter was supported by National Key Research and Development Program of China (No. 2021YFA1400900), the National Natural Science Foundation of China (Grants No. 11825401, No. 12261160368, and No. 11921005), and the Innovation Program for Quantum Science and Technology (Grant No. 2021ZD0302000). Long Zhang also acknowledges support from the startup grant of the Huazhong University of Science and Technology (Grant No. 3004012191). Lin Zhang also acknowledges support from ERC AdG NOQIA; Ministerio de Ciencia y Innovation Agencia Estatal de Investigaciones (No. PGC2018-097027-B-I00/10.13039/501100011033, No. CEX2019-000910-S/10.13039/501100011033, Plan National FIDEUA No. PID2019-106901GB-I00, FPI, QUANTERA MAQS No. PCI2019-111828-2, QUANTERA DYNAMITE No. PCI2022-132919, Proyectos de I+D+I "Retos Colaboración" QUSPIN No. RTC2019-007196-7); MICIIN with funding from European Union NextGenerationEU (No. PRTR-C17.I1) and by Generalitat de Catalunya; Fundació Cellex; Fundació Mir-Puig; Generalitat de Catalunya (European Social Fund FEDER and CERCA program, AGAUR Grant No. 2021 SGR 01452, QuantumCAT\U16-011424, co-funded by ERDF Operational Program of Catalonia 2014–2020); Barcelona Supercomputing Center MareNostrum (No. FI-2022-1-0042); EU (PASQuanS2.1, 101113690); EU Horizon 2020 FET-OPEN OPTOlogic (Grant No. 899794); EU Horizon Europe Program (Grant Agreement No. 101080086—NeQST), National Science Centre, Poland (Symfonia Grant No. 2016/20/W/ST4/00314); ICFO Internal "QuantumGaudi" project; European Union's Horizon 2020 research and innovation program under the Marie-Skłodowska-Curie Grant Agreement No. 101029393 (STREDCH) and No. 847648 ("La Caixa" Junior Leaders fellowships ID100010434: No. LCF/BQ/PI19/11690013, No. LCF/BQ/PI20/11760031, No. LCF/BQ/PR20/11770012, and No. LCF/BQ/PR21/11840013). Views and opinions expressed in this work are, however, those of the author(s) only and do not necessarily reflect those of the European Union, European Commission, European Climate, Infrastructure and Environment Executive Agency, nor any other granting authority. Neither the European Union nor any granting authority can be held responsible for them.

[1] M. Sitte, A. Rosch, E. Altman, and L. Fritz, Topological Insulators in Magnetic Fields: Quantum Hall Effect and Edge Channels with a Nonquantized θ Term, Phys. Rev. Lett. **108**, 126807 (2012).

[2] F. Zhang, C. L. Kane, and E. J. Mele, Surface State Magnetization and Chiral Edge States on Topological Insulators, Phys. Rev. Lett. **110**, 046404 (2013).

[3] W. A. Benalcazar, B. A. Bernevig, and T. L. Hughes, Quantized electric multipole insulators, Science **357**, 61 (2017).

[4] Z. Song, Z. Fang, and C. Fang, $(d-2)$-Dimensional Edge States of Rotation Symmetry Protected Topological States, Phys. Rev. Lett. **119**, 246402 (2017).

[5] Q. Wang, C.-C. Liu, Y.-M. Lu, and F. Zhang, High-Temperature Majorana Corner States, Phys. Rev. Lett. **121**, 186801 (2018).

[6] Z. Yan, F. Song, and Z. Wang, Majorana Corner Modes in a High-Temperature Platform, Phys. Rev. Lett. **121**, 096803 (2018).

[7] R.-J. Slager, L. Rademaker, J. Zaanen, and L. Balents, Impurity-bound states and Green's function zeros as local signatures of topology, Phys. Rev. B **92**, 085126 (2015).

[8] W. A. Benalcazar, B. A. Bernevig, and T. L. Hughes, Electric multipole moments, topological multipole moment pumping, and chiral hinge states in crystalline insulators, Phys. Rev. B **96**, 245115 (2017).

[9] F. Liu and K. Wakabayashi, Novel Topological Phase with a Zero Berry Curvature, Phys. Rev. Lett. **118**, 076803 (2017).

[10] J. Langbehn, Y. Peng, L. Trifunovic, F. von Oppen, and P. W. Brouwer, Reflection-Symmetric Second-Order Topological Insulators and Superconductors, Phys. Rev. Lett. **119**, 246401 (2017).

[11] L. Li, H. H. Yap, M. A. N. Araújo, and J. Gong, Engineering topological phases with a three-dimensional nodal-loop semimetal, Phys. Rev. B **96**, 235424 (2017).

[12] F. Schindler, A. M. Cook, M. G. Vergniory, Z. Wang, S. S. Parkin, B. A. Bernevig, and T. Neupert, Higher-order topological insulators, Sci. Adv. **4**, eaat0346 (2018).

[13] M. Ezawa, Higher-Order Topological Insulators and Semimetals on the Breathing Kagome and Pyrochlore Lattices, Phys. Rev. Lett. **120**, 026801 (2018).

[14] M. Ezawa, Topological Switch between Second-Order Topological Insulators and Topological Crystalline Insulators, Phys. Rev. Lett. **121**, 116801 (2018).

[15] E. Khalaf, Higher-order topological insulators and superconductors protected by inversion symmetry, Phys. Rev. B **97**, 205136 (2018).

[16] M. Geier, L. Trifunovic, M. Hoskam, and P. W. Brouwer, Second-order topological insulators and superconductors with an order-two crystalline symmetry, Phys. Rev. B **97**, 205135 (2018).

[17] R. Queiroz and A. Stern, Splitting the Hinge Mode of Higher-Order Topological Insulators, Phys. Rev. Lett. **123**, 036802 (2019).

[18] X.-L. Sheng, C. Chen, H. Liu, Z. Chen, Z.-M. Yu, Y. X. Zhao, and S. A. Yang, Two-Dimensional Second-Order Topological Insulator in Graphdiyne, Phys. Rev. Lett. **123**, 256402 (2019).

[19] L. Trifunovic and P. W. Brouwer, Higher-Order Bulk-Boundary Correspondence for Topological Crystalline Phases, Phys. Rev. X **9**, 011012 (2019).

[20] D. Călugăru, V. Juričić, and B. Roy, Higher-order topological phases: A general principle of construction, Phys. Rev. B **99**, 041301(R) (2019).

[21] M. J. Park, Y. Kim, G. Y. Cho, and S. B. Lee, Higher-Order Topological Insulator in Twisted Bilayer Graphene, Phys. Rev. Lett. **123**, 216803 (2019).

[22] W. A. Benalcazar, T. Li, and T. L. Hughes, Quantization of fractional corner charge in C_n-symmetric higher-order topological crystalline insulators, Phys. Rev. B **99**, 245151 (2019).

[23] Z. Yan, Higher-Order Topological Odd-Parity Superconductors, Phys. Rev. Lett. **123**, 177001 (2019).

[24] X. Zhu, Second-Order Topological Superconductors with Mixed Pairing, Phys. Rev. Lett. **122**, 236401 (2019).

[25] X.-H. Pan, K.-J. Yang, L. Chen, G. Xu, C.-X. Liu, and X. Liu, Lattice-Symmetry-Assisted Second-Order Topological Superconductors and Majorana Patterns, Phys. Rev. Lett. **123**, 156801 (2019).

[26] Y. Volpez, D. Loss, and J. Klinovaja, Second-Order Topological Superconductivity in π-Junction Rashba Layers, Phys. Rev. Lett. **122**, 126402 (2019).

[27] C. Zeng, T. D. Stanescu, C. Zhang, V. W. Scarola, and S. Tewari, Majorana Corner Modes with Solitons in an Attractive Hubbard-Hofstadter Model of Cold Atom Optical Lattices, Phys. Rev. Lett. **123**, 060402 (2019).

[28] Y. Ren, Z. Qiao, and Q. Niu, Engineering Corner States from Two-Dimensional Topological Insulators, Phys. Rev. Lett. **124**, 166804 (2020).

[29] A. Tiwari, M.-H. Li, B. A. Bernevig, T. Neupert, and S. A. Parameswaran, Unhinging the Surfaces of Higher-Order Topological Insulators and Superconductors, Phys. Rev. Lett. **124**, 046801 (2020).

[30] R.-X. Zhang, F. Wu, and S. Das Sarma, Möbius Insulator and Higher-Order Topology in $MnBi_{2n}Te_{3n+1}$, Phys. Rev. Lett. **124**, 136407 (2020).

[31] E. Lee, R. Kim, J. Ahn, and B.-J. Yang, Two-dimensional higher-order topology in monolayer graphdiyne, npj Quantum Mater. **5**, 1 (2020).

[32] L. Trifunovic and P. W. Brouwer, Higher-order topological band structures, Phys. Status Solidi B **258**, 2000090 (2021).

[33] Y. Tan, Z.-H. Huang, and X.-J. Liu, Two-particle Berry phase mechanism for Dirac and Majorana Kramers pairs of corner modes, Phys. Rev. B **105**, L041105 (2022).

[34] Y. Peng and G. Refael, Floquet Second-Order Topological Insulators from Nonsymmorphic Space-Time Symmetries, Phys. Rev. Lett. **123**, 016806 (2019).

[35] B. Huang and W. V. Liu, Floquet Higher-Order Topological Insulators with Anomalous Dynamical Polarization, Phys. Rev. Lett. **124**, 216601 (2020).

[36] H. Hu, B. Huang, E. Zhao, and W. V. Liu, Dynamical Singularities of Floquet Higher-Order Topological Insulators, Phys. Rev. Lett. **124**, 057001 (2020).

[37] X.-W. Luo and C. Zhang, Higher-Order Topological Corner States Induced by Gain and Loss, Phys. Rev. Lett. **123**, 073601 (2019).

[38] C. H. Lee, L. Li, and J. Gong, Hybrid Higher-Order Skin-Topological Modes in Nonreciprocal Systems, Phys. Rev. Lett. **123**, 016805 (2019).

[39] Z. Zhang, M. Rosendo López, Y. Cheng, X. Liu, and J. Christensen, Non-Hermitian Sonic Second-Order Topological Insulator, Phys. Rev. Lett. **122**, 195501 (2019).

[40] T. Liu, Y.-R. Zhang, Q. Ai, Z. Gong, K. Kawabata, M. Ueda, and F. Nori, Second-Order Topological Phases in Non-Hermitian Systems, Phys. Rev. Lett. **122**, 076801 (2019).

[41] A. A. Stepanenko, M. D. Lyubarov, and M. A. Gorlach, Higher-Order Topological Phase of Interacting Photon Pairs, Phys. Rev. Lett. **128**, 213903 (2022).

[42] J. May-Mann, Y. You, T. L. Hughes, and Z. Bi, Interaction enabled fractonic higher-order topological phases, Phys. Rev. B **105**, 245122 (2022).

[43] Z. Yang, E. Lustig, Y. Lumer, and M. Segev, Photonic Floquet topological insulators in a fractal lattice, Light Sci. Appl. **9**, 128 (2020).

[44] S. Zheng, X. Man, Z.-L. Kong, Z.-K. Lin, G. Duan, N. Chen, D. Yu, J.-H. Jiang, and B. Xia, Observation of fractal higher-order topological states in acoustic metamaterials, Sci. Bull. **67**, 2069 (2022).

[45] S. A. A. Ghorashi, T. L. Hughes, and E. Rossi, Vortex and Surface Phase Transitions in Superconducting Higher-order Topological Insulators, Phys. Rev. Lett. **125**, 037001 (2020).

[46] M. Kheirkhah, Z. Yan, Y. Nagai, and F. Marsiglio, First- and Second-Order Topological Superconductivity and Temperature-Driven Topological Phase Transitions in the Extended Hubbard Model with Spin-Orbit Coupling, Phys. Rev. Lett. **125**, 017001 (2020).

[47] C.-A. Li, B. Fu, Z.-A. Hu, J. Li, and S.-Q. Shen, Topological Phase Transitions in Disordered Electric Quadrupole Insulators, Phys. Rev. Lett. **125**, 166801 (2020).

[48] X. Wu, W. A. Benalcazar, Y. Li, R. Thomale, C.-X. Liu, and J. Hu, Boundary-Obstructed Topological High-T_c Superconductivity in Iron Pnictides, Phys. Rev. X **10**, 041014 (2020).

[49] M. Ezawa, Edge-corner correspondence: Boundary-obstructed topological phases with chiral symmetry, Phys. Rev. B **102**, 121405(R) (2020).

[50] K. Asaga and T. Fukui, Boundary-obstructed topological phases of a massive Dirac fermion in a magnetic field, Phys. Rev. B **102**, 155102 (2020).

[51] J. Claes and T. L. Hughes, Wannier band transitions in disordered π-flux ladders, Phys. Rev. B **102**, 100203(R) (2020).

[52] E. Khalaf, W. A. Benalcazar, T. L. Hughes, and R. Queiroz, Boundary-obstructed topological phases, Phys. Rev. Res. **3**, 013239 (2021).

[53] Y.-B. Yang, K. Li, L.-M. Duan, and Y. Xu, Type-II quadrupole topological insulators, Phys. Rev. Res. **2**, 033029 (2020).

[54] J. Du, T. Li, X. Fan, Q. Zhang, and C. Qiu, Acoustic Realization of Surface-Obstructed Topological Insulators, Phys. Rev. Lett. **128**, 224301 (2022).

[55] N. Mao, R. Li, Y. Dai, B. Huang, B. Yan, and C. Niu, Orbital shift-induced boundary obstructed topological materials with a large energy gap, Adv. Sci. **9**, 2202564 (2022).

[56] J.-H. Chen, Z.-Z. Yang, W.-J. Yang, A.-Y. Guan, X.-Y. Zou, and J.-C. Cheng, Experimental realization of boundary-obstructed topological insulators using acoustic two-dimensional Su–Schrieffer–Heeger network, Appl. Phys. Lett. **120**, 253508 (2022).

[57] N. Marzari, A. A. Mostofi, J. R. Yates, I. Souza, and D. Vanderbilt, Maximally localized Wannier functions: Theory and applications, Rev. Mod. Phys. **84**, 1419 (2012).

[58] Y. Yang, J. Lu, M. Yan, X. Huang, W. Deng, and Z. Liu, Hybrid-Order Topological Insulators in a Phononic Crystal, Phys. Rev. Lett. **126**, 156801 (2021).

[59] W. A. Benalcazar and A. Cerjan, Chiral-Symmetric Higher-Order Topological Phases of Matter, Phys. Rev. Lett. **128**, 127601 (2022).

[60] X.-J. Luo, X.-H. Pan, C.-X. Liu, and X. Liu, Higher-order topological phases emerging from Su-Schrieffer-Heeger stacking, Phys. Rev. B **107**, 045118 (2023).

[61] A. Cerjan, M. Jürgensen, W. A. Benalcazar, S. Mukherjee, and M. C. Rechtsman, Observation of a Higher-Order Topological Bound State in the Continuum, Phys. Rev. Lett. **125**, 213901 (2020).

[62] J. Niu, T. Yan, Y. Zhou, Z. Tao, X. Li, W. Liu, L. Zhang, H. Jia, S. Liu, Z. Yan *et al.*, Simulation of higher-order topological phases and related topological phase transitions in a superconducting qubit, Sci. Bull. **66**, 1168 (2021).

[63] B. Xie, H.-X. Wang, X. Zhang, P. Zhan, J.-H. Jiang, M. Lu, and Y. Chen, Higher-order band topology, Nat. Rev. Phys. **3**, 520 (2021).

[64] M. Serra-Garcia, V. Peri, R. Süsstrunk, O. R. Bilal, T. Larsen, L. G. Villanueva, and S. D. Huber, Observation of a phononic quadrupole topological insulator, Nature (London) **555**, 342 (2018).

[65] C. W. Peterson, W. A. Benalcazar, T. L. Hughes, and G. Bahl, A quantized microwave quadrupole insulator with topologically protected corner states, Nature (London) **555**, 346 (2018).

[66] S. Imhof, C. Berger, F. Bayer, J. Brehm, L. W. Molenkamp, T. Kiessling, F. Schindler, C. H. Lee, M. Greiter, T. Neupert *et al.*, Topolectrical-circuit realization of topological corner modes, Nat. Phys. **14**, 925 (2018).

[67] X. Ni, M. Weiner, A. Alu, and A. B. Khanikaev, Observation of higher-order topological acoustic states protected by generalized chiral symmetry, Nat. Mater. **18**, 113 (2019).

[68] H. Fan, B. Xia, L. Tong, S. Zheng, and D. Yu, Elastic Higher-Order Topological Insulator with Topologically Protected Corner States, Phys. Rev. Lett. **122**, 204301 (2019).

[69] H. Xue, Y. Yang, F. Gao, Y. Chong, and B. Zhang, Acoustic higher-order topological insulator on a kagome lattice, Nat. Mater. **18**, 108 (2019).

[70] A. El Hassan, F. K. Kunst, A. Moritz, G. Andler, E. J. Bergholtz, and M. Bourennane, Corner states of light in photonic waveguides, Nat. Photonics **13**, 697 (2019).

[71] S. Kempkes, M. Slot, J. van Den Broeke, P. Capiod, W. Benalcazar, D. Vanmaekelbergh, D. Bercioux, I. Swart, and C. M. Smith, Robust zero-energy modes in an electronic higher-order topological insulator, Nat. Mater. **18**, 1292 (2019).

[72] Q. Wei, X. Zhang, W. Deng, J. Lu, X. Huang, M. Yan, G. Chen, Z. Liu, and S. Jia, 3D Hinge Transport in Acoustic Higher-Order Topological Insulators, Phys. Rev. Lett. **127**, 255501 (2021).

[73] I. Bloch, J. Dalibard, and S. Nascimbene, Quantum simulations with ultracold quantum gases, Nat. Phys. **8**, 267 (2012).

[74] G. Jotzu, M. Messer, R. Desbuquois, M. Lebrat, T. Uehlinger, D. Greif, and T. Esslinger, Experimental realization of the topological Haldane model with ultracold fermions, Nature (London) **515**, 237 (2014).

[75] Z. Wu, L. Zhang, W. Sun, X.-T. Xu, B.-Z. Wang, S.-C. Ji, Y. Deng, S. Chen, X.-J. Liu, and J.-W. Pan, Realization of two-dimensional spin-orbit coupling for Bose-Einstein condensates, Science **354**, 83 (2016).

[76] F. Schäfer, T. Fukuhara, S. Sugawa, Y. Takasu, and Y. Takahashi, Tools for quantum simulation with ultracold atoms in optical lattices, Nat. Rev. Phys. **2**, 411 (2020).

[77] F. Kong, C. Ju, Y. Liu, C. Lei, M. Wang, X. Kong, P. Wang, P. Huang, Z. Li, F. Shi *et al.*, Direct Measurement of Topological Numbers with Spins in Diamond, Phys. Rev. Lett. **117**, 060503 (2016).

[78] A. Ariyaratne, D. Bluvstein, B. A. Myers, and A. C. B. Jayich, Nanoscale electrical conductivity imaging using a nitrogen-vacancy center in diamond, Nat. Commun. **9**, 2406 (2018).

[79] W. Ji, L. Zhang, M. Wang, L. Zhang, Y. Guo, Z. Chai, X. Rong, F. Shi, X.-J. Liu, Y. Wang *et al.*, Quantum Simulation for Three-Dimensional Chiral Topological Insulator, Phys. Rev. Lett. **125**, 020504 (2020).

[80] T. Xin, Y. Li, Y.-a. Fan, X. Zhu, Y. Zhang, X. Nie, J. Li, Q. Liu, and D. Lu, Quantum Phases of Three-Dimensional Chiral Topological Insulators on a Spin Quantum Simulator, Phys. Rev. Lett. **125**, 090502 (2020).

[81] D. Zhao, C. Wei, S. Xue, Y. Huang, X. Nie, J. Li, D. Ruan, D. Lu, T. Xin, and G. Long, Characterizing quantum simulations with quantum tomography on a spin quantum simulator, Phys. Rev. A **103**, 052403 (2021).

[82] L. Zhang, L. Zhang, S. Niu, and X.-J. Liu, Dynamical classification of topological quantum phases, Sci. Bull. **63**, 1385 (2018).

[83] B. Song, C. He, S. Niu, L. Zhang, Z. Ren, X.-J. Liu, and G.-B. Jo, Observation of nodal-line semimetal with ultracold fermions in an optical lattice, Nat. Phys. **15**, 911 (2019).

[84] J. Ye and F. Li, Emergent topology under slow nonadiabatic quantum dynamics, Phys. Rev. A **102**, 042209 (2020).

[85] L. Zhang, L. Zhang, and X.-J. Liu, Unified Theory to Characterize Floquet Topological Phases by Quench Dynamics, Phys. Rev. Lett. **125**, 183001 (2020).

[86] X.-L. Yu, W. Ji, L. Zhang, Y. Wang, J. Wu, and X.-J. Liu, Quantum dynamical characterization and simulation of topological phases with high-order band inversion surfaces, Phys. Rev. X Quantum **2**, 020320 (2021).

[87] L. Li, W. Zhu, and J. Gong, Direct dynamical characterization of higher-order topological phases with nested band inversion surfaces, Sci. Bull. **66**, 1502 (2021).

[88] Z.-Y. Wang, X.-C. Cheng, B.-Z. Wang, J.-Y. Zhang, Y.-H. Lu, C.-R. Yi, S. Niu, Y. Deng, X.-J. Liu, S. Chen *et al.*, Realization of an ideal Weyl semimetal band in a quantum gas with 3D spin-orbit coupling, Science **372**, 271 (2021).

[89] B. Chen, S. Li, X. Hou, F. Ge, F. Zhou, P. Qian, F. Mei, S. Jia, N. Xu, and H. Shen, Digital quantum simulation of Floquet topological phases with a solid-state quantum simulator, Photon. Res. **9**, 81 (2021).

[90] L. Zhang, W. Jia, and X.-J. Liu, Universal topological quench dynamics for $\mathbb{Z}_2$ topological phases, Sci. Bull. **67**, 1236 (2022).

[91] Z. Lei, Y. Deng, and L. Li, Topological classification of higher-order topological phases with nested band inversion surfaces, Phys. Rev. B **106**, 245105 (2022).

[92] T. Morimoto and A. Furusaki, Topological classification with additional symmetries from Clifford algebras, Phys. Rev. B **88**, 125129 (2013).

[93] C.-K. Chiu, H. Yao, and S. Ryu, Classification of topological insulators and superconductors in the presence of reflection symmetry, Phys. Rev. B **88**, 075142 (2013).

[94] W.-P. Su, J. R. Schrieffer, and A. J. Heeger, Soliton excitations in polyacetylene, Phys. Rev. B **22**, 2099 (1980).

[95] F. D. M. Haldane, Model for a Quantum Hall Effect without Landau Levels: Condensed-Matter Realization of the "Parity Anomaly", Phys. Rev. Lett. **61**, 2015 (1988).

[96] R. Jackiw and C. Rebbi, Solitons with fermion number $\frac{1}{2}$, Phys. Rev. D **13**, 3398 (1976).

[97] See Supplemental Material at http://link.aps.org/supplemental/10.1103/PhysRevResearch.5.L022032 for details on (I) MDW-BIS duality and its applications, (II) HOTPTs, and (III) dynamical characterization in the 2D second-order, 3D second-order, and 3D third-order TIs, which includes Refs. [82,86,93,99,99,100,102].

[98] For the example of $\mathcal{H}_{\mathbf{k}^{(i-1)}}$ perpendicular to the $k_d \cdots k_{d-i+2}$ direction, it can be obtained by projecting $\mathcal{H}_{\mathbf{k}}$ with $n = i$ as $\mathcal{H}_{\mathbf{k}^{(i-1)}} = \mathbf{P}^{(i-2)^\dagger} \cdots \mathbf{P}^{(0)^\dagger} \mathcal{H}_{\mathbf{k}} \mathbf{P}^{(0)} \cdots \mathbf{P}^{(i-2)}$, where $\mathcal{H}_{\mathbf{k}^{(0)}} = \mathcal{H}_{\mathbf{k}}$. The projection operator is $\mathbf{P}^{(i-1)} = [1 - \mathrm{i}\gamma_{d+i}^{(i-1)} \gamma_{d-i+1}^{(i-1)}]/2$ in the eigenspace of $i\gamma_{d+i}^{(i-1)} \gamma_{d-i+1}^{(i-1)} = -1$, where $\boldsymbol{\gamma}^{(i)} = \mathbf{P}^{(i-1)^\dagger} \boldsymbol{\gamma}^{(i-1)} \mathbf{P}^{(i-1)}$ has the half size of $\boldsymbol{\gamma}^{(i-1)}$.

[99] R. S. K. Mong and V. Shivamoggi, Edge states and the bulk-boundary correspondence in Dirac Hamiltonians, Phys. Rev. B **83**, 125109 (2011).

[100] F. K. Kunst, M. Trescher, and E. J. Bergholtz, Anatomy of topological surface states: Exact solutions from destructive interference on frustrated lattices, Phys. Rev. B **96**, 085443 (2017).

[101] L. Zhang, L. Zhang, and X.-J. Liu, Characterizing topological phases by quantum quenches: A general theory, Phys. Rev. A **100**, 063624 (2019).

[102] W. Jia, L. Zhang, L. Zhang, and X.-J. Liu, Dynamically characterizing topological phases by high-order topological charges, Phys. Rev. A **103**, 052213 (2021).

[103] L. Zhou, Generating many Majorana corner modes and multiple phase transitions in Floquet second-order topological superconductors, Symmetry **14**, 2546 (2022).